



An iron-containing nanomedicine for inducing deep tumor penetration and synergistic ferroptosis in enhanced pancreatic cancer therapy

Aiping Huang^{a,c,1}, Qingnian Li^{a,1}, Xinyi Shi^{a,d}, Junyi Gao^b, Yiran Ma^e, Jinsong Ding^a, Surong Hua^{b,**}, Wenhui Zhou^{a,*}

^a Xiangya School of Pharmaceutical Sciences, Central South University, Changsha, Hunan, 410013, China

^b Department of General Surgery, State Key Laboratory of Complex Severe and Rare Diseases, Peking Union Medical College Hospital, Chinese Academy of Medical Science and Peking Union Medical College, Beijing, China

^c The Second Affiliated Hospital of Guangxi Medical University, Nanning, Guangxi, 530007, China

^d Department of Pharmacy, Haikou Affiliated Hospital of Central South University Xiangya School of Medicine (Haikou People's Hospital), Haikou, Hainan, 570208, China

^e Hunan Prize Life Science Research Institute Co., LTD, China

ARTICLE INFO

Keywords:

Nanomedicine
Metal-organic-frameworks
Macrophage polarization
Fibroblast activation
Fenton reaction

ABSTRACT

Pancreatic cancer is an aggressive and challenging malignancy with limited treatment options, largely attributed to the dense tumor stroma and intrinsic drug resistance. Here, we introduce a novel iron-containing nanoparticle formulation termed PTFE, loaded with the ferroptosis inducer Erastin, to overcome these obstacles and enhance pancreatic cancer therapy. The PTFE nanoparticles were prepared through a one-step assembly process, consisting of an Erastin-loaded PLGA core stabilized by a MOF shell formed by coordination between Fe³⁺ and tannic acid. PTFE demonstrated a unique capability to repolarize tumor-associated macrophages (TAMs) into the M1 phenotype, leading to the regulation of dense tumor stroma by modulating the activation of tumor-associated fibroblasts (TAFs) and reducing collagen deposition. This resulted in enhanced nanoparticle accumulation and deep penetration, as confirmed by *in vitro* multicellular tumor spheroids and *in vivo* mesenchymal-rich subcutaneous pancreatic tumor models. Moreover, PTFE effectively combated tumor resistance by synergistically employing the Fe³⁺-induced Fenton reaction and Erastin-induced ferroptosis, thereby disrupting the redox balance. As a result, significant tumor growth inhibition was achieved in mice-bearing tumor model. Comprehensive safety evaluations demonstrated PTFE's favorable biocompatibility, highlighting its potential as a promising therapeutic platform to effectively address the formidable challenges in pancreatic cancer treatment.

1. Introduction

Pancreatic cancer is a devastating malignancy with a dismal prognosis, characterized by aggressive tumor growth and a high rate of treatment resistance [1,2]. Despite advances in cancer therapy, the current standard chemotherapy, such as gemcitabine, offers limited efficacy, primarily attributed to the prevalence of K-RAS gene mutations in pancreatic cancer cells, rendering them highly resistant to conventional drugs [3,4]. Consequently, the urgent need to identify novel treatment strategies to improve patient survival and overcome therapeutic obstacles in pancreatic cancer remains paramount.

In recent years, extensive research has delved into understanding the pathological intricacies of pancreatic cancer, with a particular focus on the tumor microenvironment (TME). Within the TME, an abundance of tumor-associated macrophages (TAMs) plays a critical role in cancer progression, fostering the activation of tumor-associated fibroblasts (TAFs) via the secretion of transforming growth factor-beta (TGF- β) [5–7]. This TAF activation process leads to the deposition of a dense stroma, constituting up to 90 % of the tumor mass, acting as a physical barrier that hampers effective drug delivery to the tumor site [8–10]. Consequently, targeting this dense stroma has emerged as a promising approach to improve therapeutic outcomes in pancreatic cancer.

* Corresponding author.

** Corresponding author.

E-mail addresses: huasurong@tsinghua.org.cn (S. Hua), zhouwenhuyaoji@163.com (W. Zhou).

¹ These authors contributed equally to this work.

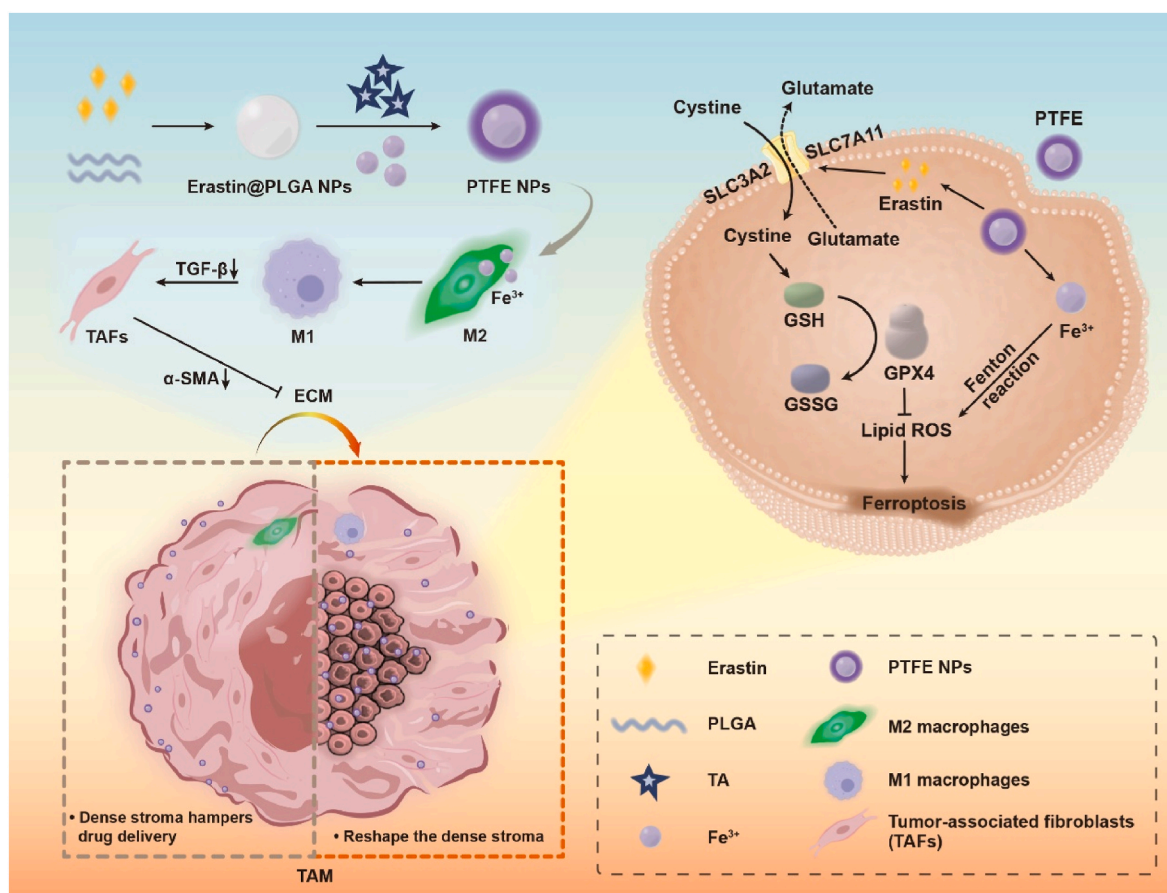
Along this direction, depletion of tumor stroma has become a popular strategy to enhance drug delivery efficiency [11,12]. For example, Chen et al. used a new type of TAFs-targeting liposome to down-regulate extracellular matrix deposition, reduce interstitial pressure and increase drug penetration efficiency [13]. However, stromal destruction poses challenges, as excessive elimination may trigger cancer cell invasion and metastasis [14]. Consequently, researchers have shifted their focus towards modulating TAFs to regulate the stromal environment, rather than complete clearance. In this regard, iron (Fe^{3+})-based nanoformulations have garnered interest due to their ability to reshape the TME and simultaneously induce chemical dynamic therapy (CDT) by generating hydroxyl radicals ($\cdot\text{OH}$) via the Fenton reaction [13,15,16]. In the context of pancreatic cancer cells, the high level of reactive oxygen species (ROS) provides a unique advantage for Fe^{3+} to enhance ROS toxicity, known as ferroptosis [17,18].

However, pancreatic cancer cells have the ability to reduce their sensitivity to ferroptosis by upregulating the xCT-GSH-GPX4 antioxidant system [19,20]. The cysteine/glutamate transporter (System Xc-, xCT) counteracts oxidative stress by transporting cysteine for glutathione (GSH) synthesis, enabling cancer cells to evade ROS accumulation. Moreover, glutathione peroxidase 4 (GPX4) further neutralizes peroxidized lipids, reducing the effectiveness of iron-induced cytotoxicity [21, 22]. Thus, addressing the resistance of pancreatic cancer cells to free radicals and optimizing their sensitivity to ferroptosis emerges as a crucial determinant of treatment efficacy.

Notably, a recent study demonstrated the potential of the ferroptosis inducer, Erastin, to selectively target pancreatic cancer cells by inhibiting the transport of cysteine via the xCT transporter [23,24]. The inhibition of xCT led to a reduction in intracellular GSH content,

disturbing the redox balance in cancer cells and ultimately inducing ferroptosis. Erastin exerts its effect as a direct xCT inhibitor, not only curtailing cysteine uptake and depleting GSH levels but also interfering with proper protein folding within the cells. Consequently, this disruption results in the accumulation of incompletely folded proteins, thereby triggering the endoplasmic reticulum stress response and further facilitating iron-induced cell death. This study highlights that the inhibitory properties of Erastin enable pancreatic cancer cells to evade the clearance of ROS and peroxidized lipids. Importantly, the relatively low intensity of oxidative stress reactions in normal cells, coupled with the presence of protective mechanisms like transsulfuration [25], renders ferroptosis induction strategies specifically target pancreatic cancer cells, holding great promise for precision cancer therapy.

Building on these findings, this study presents a novel iron-containing nanoparticle formulation loaded with Erastin, termed PTFE, for enhanced pancreatic therapy (see Scheme 1). The nanoparticle structure comprises a nano-core of Erastin encapsulated within PLGA, and an outer MOF shell formed through Fe^{3+} coordination with tannic acid (TA). In view of the dense interstitial drug resistance of pancreatic cancer, the PTFE designed in this study regulates TAFs and tumor dense matrix by inducing M2-M1 polarization of macrophages through the synergistic action of Fe^{3+} and Erastin, thereby improving nanoparticle permeability and overcoming drug delivery barriers. Meanwhile, the formulation disrupts the redox balance at the tumor site, inducing ferroptosis in cancer cells, and presents a promising therapeutic strategy for pancreatic cancer. In vivo and in vitro results have demonstrated the efficacy of PTFE in treating pancreatic cancer, with its ability to facilitate deep tumor penetration, induce tumor ferroptosis, and maintain favorable biocompatibility, positioning it as a promising therapeutic



Scheme 1. Schematic illustration of the preparation and mechanism of action for the PTFE. Ferroptosis inducer Erastin is encapsulated by a MOF shell formed by Fe^{3+} coordination with TA to eventually form PTFE. PTFE regulates TAFs and tumor dense stroma by inducing macrophage polarization, thereby improving nanoparticle permeability. Meanwhile, PTFE disrupts the redox balance at the tumor site and induces pronounced ferroptotic damage.

platform to address the formidable challenges in pancreatic cancer treatment.

2. Results and discussion

2.1. Preparation and characterization PTFE NPs

The synthesis of PTFE nanoparticles was achieved through a self-assembly process, as depicted in Fig. 1A. Briefly, a solution containing PLGA, Erastin, and Fe^{3+} in acetone was added to an aqueous solution containing TA. Subsequently, organic solvent evaporation and Fe^{3+} /TA coordination led to the formation of PTFE nanoparticles. Erastin, being a hydrophobic drug, is encapsulated within the PLGA nanocore due to hydrophobic interactions. Subsequently, tannic acid coordinates with Fe^{3+} to form a stable MOF structure on the surface of the PLGA nanocore. This results in core-shell nanoparticles where the hydrophobic Erastin is effectively encapsulated and protected within the PLGA core, while the MOF structure stabilizes the surface and facilitates controlled drug release. For comparison, two control nanoparticle formulations, the Erastin-free nanoparticles (PTF NPs) and Erastin-loaded PLGA nanoparticles (PE NPs), were also prepared using a similar method. The nanoparticle formulation was optimized for Erastin feeding concentration (Table S1). During this optimization, it was observed that the size of the nanoparticles gradually increased and then aggregated with higher concentrations of Erastin. Consequently, the optimal Erastin feeding concentration was determined to be 20 μL (12 mg/mL). This concentration ensured the stability and homogeneity of the nanoparticles without causing aggregation. PE NPs appeared as a milky white solution, while PTF NPs and PTFE NPs exhibited a dark purple color, characteristic of the MOF structure formed by TA/ Fe^{3+} coordination (Fig. 1B) [26–28]. All nanoparticle types had comparable particle sizes ranging from 150 to 200 nm, with a low polydispersity index (PDI) of less than 0.2 (Fig. 1C). PE nanoparticles had a slightly negative surface charge of approximately -5 mV, whereas both PTF and PTFE nanoparticles exhibited a more negative surface charge, likely due to the surface MOF coating (Fig. 1D).

Transmission electron microscopy (TEM) images revealed that PE NPs appeared as homogeneous spherical solid nanoparticles, whereas PTF NPs showed a distinct framework with irregular shape. In contrast, PTFE NPs exhibited a regular spherical core-shell structure with a particle size of approximately 170 nm and a shell thickness of about 30 nm (Fig. 1E). High-angle annular dark-field scanning transmission electron microscopy (HAADF-STEM-EDS) elemental mapping confirmed that Fe was primarily distributed at the peripheral region of the nanoparticles, indicating the presence of the MOF shell layer (Fig. 1F). This is further confirmed by the UV-Vis spectra, where both PTF and PTFE show absorption peaks specific to the MOF structure at 300 nm compared to the PE NPs. The absorption peaks at 270 nm are slightly red-shifted for PTFE compared to PTF, likely due to the enhancement of the conjugation of the MOF structure by the incorporation of Erastin. (Fig. 1G). The presence of the Cl element in the structure demonstrated the successful loading of Erastin. For quantitative analysis, HPLC and ICP-OES were performed to determine the Erastin and Fe contents, which were calculated to be 7.85 % and 11.54 %, respectively.

The surface MOF coating of PTFE NPs contributed to their high colloidal stability in various biological media, such as PBS buffer and DMEM (Fig. 1H). This is due to the fact that MOF is a cross-linked network structure formed by the synergistic action of organic units and inorganic metal particles, and the carrier itself has certain stability. At the same time, MOF is also a charged three-dimensional network structure, which has electrostatic repulsion with each other, our experimental results (Fig. 1D). It is also proved that the MOF structure in this experiment is negatively charged, which reduces the collision of drug molecules, delays the aggregation and sedimentation of drugs in solution, and improves the stability of colloids. However, in DMEM (10 % FBS), the particle size of the nanoparticles increases slightly, which is

due to the adsorption of serum proteins on the surface when the nanoparticles come into contact with serum proteins, forming a protein corona. This results in an increase in hydrated particle size. To further determine the storage stability, the change of Erastin was monitored by HPLC (Fig. S1). Over 6 days of storage, no significant changes in spectra were observed, demonstrating the high stability of Erastin within the nanoparticles. This stability may be attributed to the encapsulation of Erastin in the PLGA core, reducing its contact with oxygen and ensuring the drug's stability. Additionally, iron ions are mainly coordinated with tannic acid to form a stable MOF structure, which does not accelerate the oxidation process of Erastin. Next, the *in vitro* drug release profile was investigated. PTFE NPs exhibited a sustained drug release property in physiological buffer with pH 7.4, with only 50 % Erastin release observed after 48 h (Fig. 1I). As the pH decreases to 6.0, drug release accelerates. Notably, when the pH further decreases to 5.5, a sharp increase in drug release is observed, with approximately 80 % of drug release occurring within 2 h. These observations suggest that under physiological conditions, the pH of the body fluid maintains around 7.4, resulting in slow drug release. However, as the drug reaches the tumor's external matrix through the enhanced permeability and retention (EPR) effect, the pH decreases to 6.0. Subsequently, upon entering the cell, in the lysosomal acidic environment (pH 5.5), the drug undergoes rapid degradation, leading to the release of Fe^{3+} and Erastin, thereby exerting their therapeutic effects. This pH-responsive profile could be attributed to the collapse of the MOF shell at acidic pH [29–31]. TEM visualization of the nanoparticle structure after different treatments confirmed the disintegration of the nanoparticles at pH 5.5 (Fig. 1J). Such a pH-responsive profile was advantageous for stable circulation *in vivo* while enabling rapid release of payloads within the tumor microenvironment and tumor cells. Additionally, along with the release of Erastin, the collapse of the MOF also resulted in the release of Fe^{3+} , triggering the Fenton reaction for the generation of reactive hydroxyl radicals ($\cdot\text{OH}$). The basic mechanism of Fe^{3+} -induced Fenton reaction is illustrated in Fig. 1K. The generation of $\cdot\text{OH}$ was confirmed through the catalytic oxidation of methylene blue (MB) with UV-Vis spectrophotometry. MB in H_2O_2 solution exhibited a characteristic blue UV-Vis absorbance over the range of 600–700 nm (Fig. 1L). The addition of Fe^{2+} , Fe^{3+} , and Fe-containing nanoparticles caused the discoloration of MB, accompanied by the disappearance of characteristic UV-Vis absorbance in the 600–700 nm range. This observation indicated that all Fe-containing nanoparticles had the capability to trigger the Fenton reaction upon the release of Fe ions.

2.2. *In vitro* antitumor effect PTFE NPs via promoting cell ferroptosis

Following the comprehensive characterization of PTFE nanoparticles, their potential antitumor efficacy was evaluated at the cellular level. Initially, the cytotoxicity of PTFE nanoparticles was investigated using KPC1199 pancreatic cancer cells from mice. Cells were exposed to different nanoparticle formulations, and the relative cell viabilities were assessed using the MTT assay (Fig. 2A). Notably, the blank carrier PTF treatment exhibited over 80 % cell survival rate in the concentration range of 0–50 μM , indicating the biocompatibility of the carrier. In contrast, PTFE and PE nanoparticles led to a gradual decrease in cell viability at higher concentrations, resulting in IC_{50} values of 7.62 μM and 11.19 μM , respectively. The underlying mechanisms of action were proposed based on the respective nanoparticle formulations. PE-induced tumor cell death was attributed to Erastin-induced ferroptosis, as depicted in Fig. 2B. Erastin, acting as a ferroptosis inducer, inhibited System Xc-, a cystine/glutamate transporter protein, resulting in a decrease in cellular GSH content. This disruption of redox homeostasis induced ferroptosis in the cancer cells. On the other hand, PTFE nanoparticles showed enhanced antitumor efficacy, likely due to the co-release of Fe^{3+} , which triggered the Fenton reaction, catalyzing the generation of ROS and promoting lipid peroxidation on the cell membrane to further promote ferroptosis.

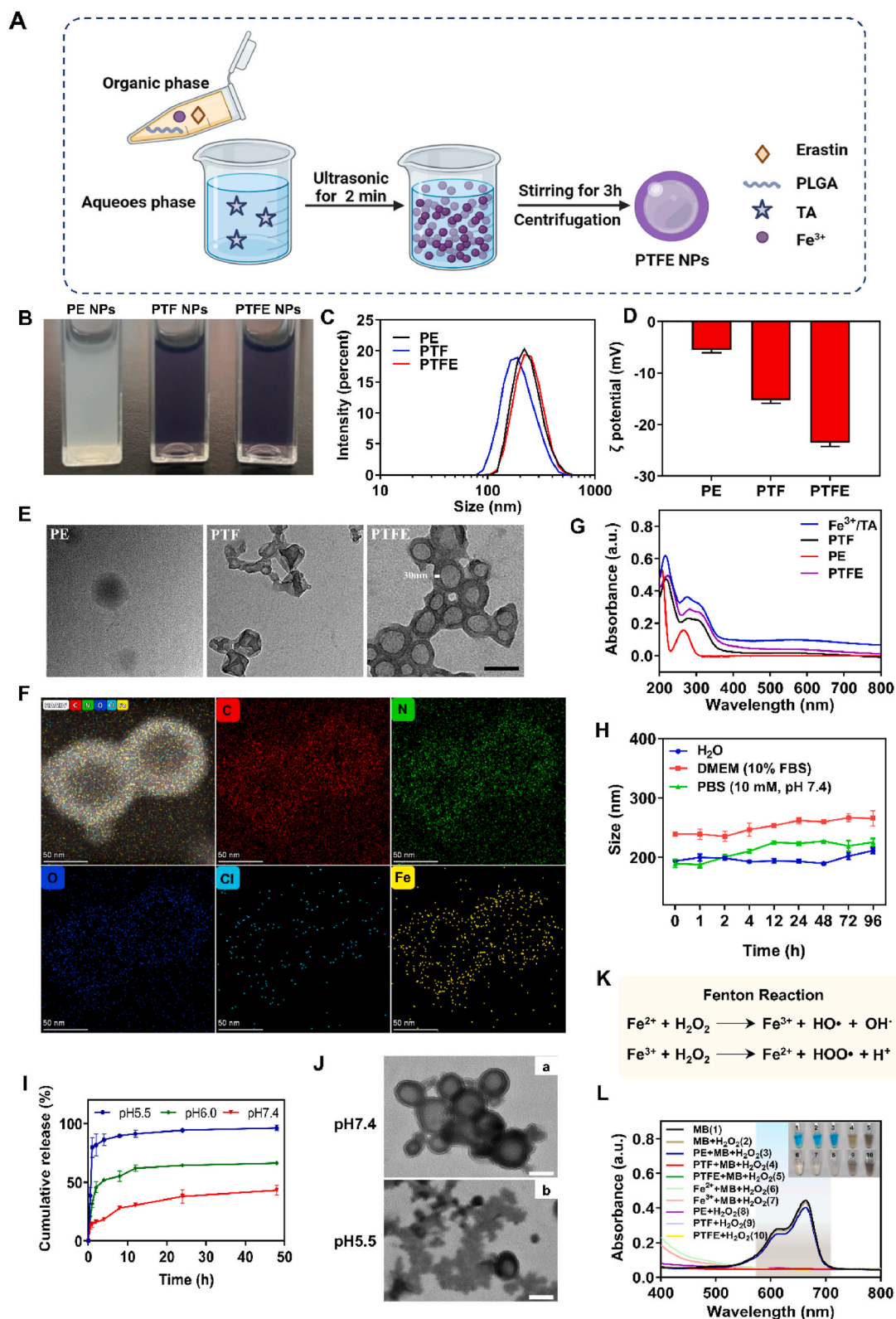


Fig. 1. Synthesis and Characterization of PTFE Nanoparticles. (A) Schematic representation of the synthesis route employed to fabricate PTFE nanoparticles via a self-assembly process. (B) Photographic images depicting the visual appearance of PE, PTF, and PTFE nanoparticles. (C) Size distribution diagram showing particle sizes of PE, PTF, and PTFE nanoparticles. (D) The ζ potential measurements of PE, PTF, and PTFE nanoparticles. (E) Transmission electron microscopy (TEM) images of the nanoparticles (scale bar: 200 nm). (F) Elemental mapping images of PTFE nanoparticles obtained by HADDF-STEM-EDS. (G) UV-Vis spectra and corresponding visual appearances of PTFE NPs, PE NPs, and Fe³⁺/TA MOF. (H) Investigation of storage stability of PTFE NPs in biological media. (I) Erastin release profile from PTFE NPs in PBS buffers at pH 7.4, pH 6.0 and pH 5.5 at room temperature. (J) TEM images of PTFE NPs at pH 7.4 and pH 5.5 for 2 h (scale bar: 100 nm). (K) Schematic representation of the Fenton effect triggered by the release of Fe³⁺ from PTFE NPs, leading to the generation of $\cdot\text{OH}$. (L) UV/Vis absorption spectra and image demonstrating the degradation of MB mediated by nanoparticles-induced Fenton effect.

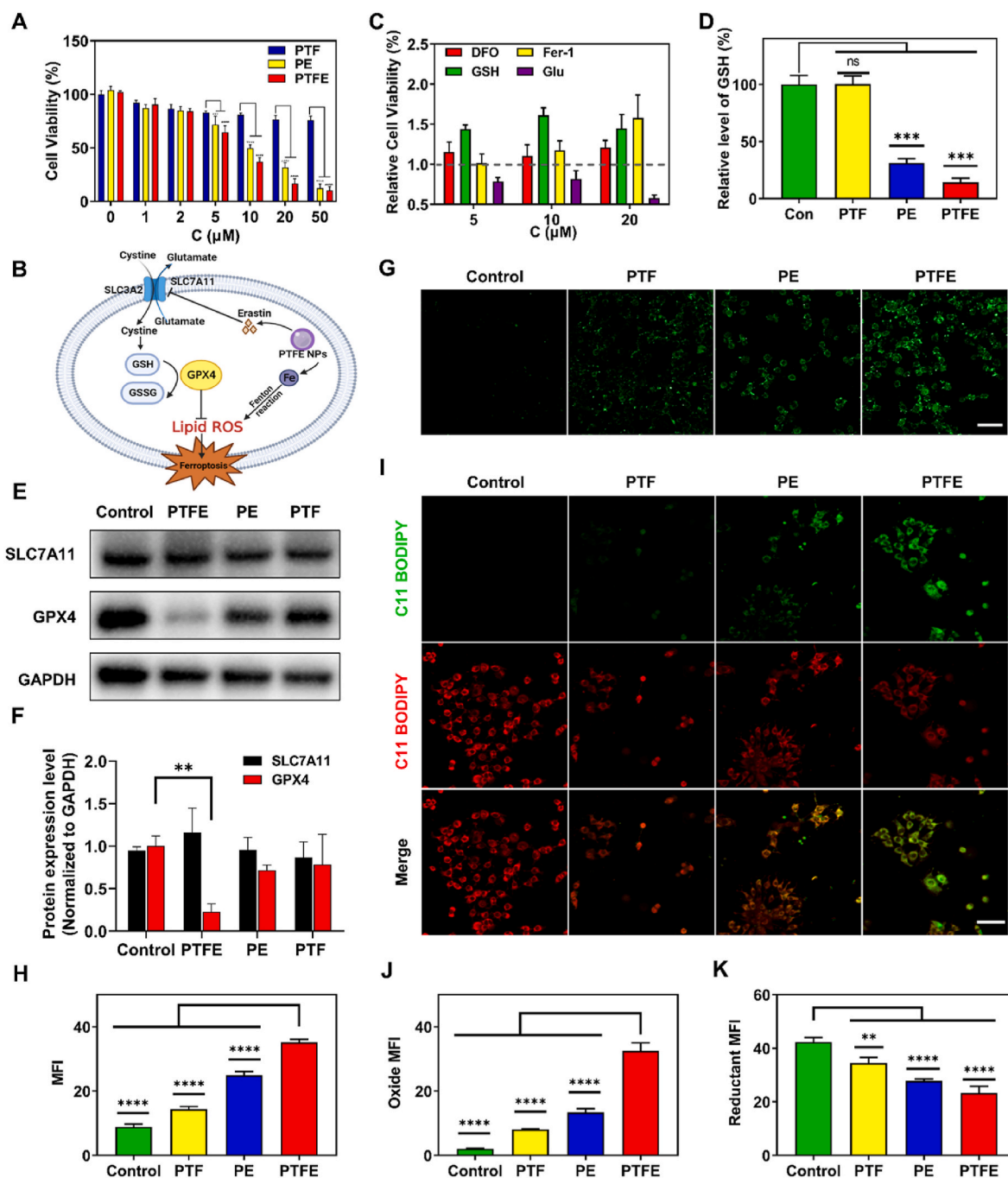


Fig. 2. Antitumor activity of PTFE nanoparticles in vitro. (A) Cytotoxicity of KPC1199 pancreatic cancer cells treated with various nanoparticles ($n = 6$). (B) Schematic representation of the mechanism of PTFE-induced ferroptosis in tumors. (C) Influence of different ferroptosis regulators on the cytotoxicity of nanoparticles ($n = 3$). (D) Intracellular GSH levels in KPC1199 cells following treatment with different nanoparticles ($n = 3$). (E) Western blot analysis of ferroptosis-related proteins in KPC1199 cells treated with different nanoparticles. (F) Relative quantitative results from E ($n = 3$). (G) Intracellular ROS levels in KPC1199 cells after treatment with different nanoparticles. Scale bar: 100 μm . (H) Relative average relative quantitative results for G ($n = 3$). (I) Intracellular LPO levels in KPC1199 cells following treatment with different nanoparticles. Scale bar: 100 μm . (J) Relative average relative quantitative results of oxidation states in I (K) Relative average relative quantitative results of the reduced state in I. Significant differences compared to the control group are indicated as ** $P < 0.01$, *** $P < 0.001$ and **** $P < 0.0001$.

To verify these mechanisms, the cell death pathway was explored by pre-treating the cells with various ferroptosis regulators before PTFE nanoparticle therapy (Fig. 2C). The results showed that ferroptosis regulators such as the iron chelator desferrioxamine (DFO), the ferroptosis inhibitor ferrostatin-1 (Fer-1), and intracellular reduced glutathione (GSH) could rescue the PTFE nanoparticle-induced cell death. DFO, as an iron chelator, binds to Fe^{3+} to form a ferric amine complex, thereby protecting it from Fe^{3+} action. The reversal of cell death by DFO

demonstrated the synergistic action of Fe^{3+} and Erastin in inducing ferroptosis. Fer-1, a potent inhibitor of ferroptosis, prevented lipid degradation through a reductive process, thereby blocking cellular ferroptosis induced by Erastin. The addition of Fer-1 reversed cell death, further confirming the major role of ferroptosis in PTFE-induced anti-tumor effects. Moreover, GSH, as a reducing agent, maintained intracellular redox balance and inhibited cell death at its root cause. The significant enhancement of cell death by the addition of glutamate (Glu)

indicated the presence of System Xc-, which mediates cystine/glutamate exchange and affects GSH synthesis, leading to oxidative cell death.

To validate the impact of PTFE nanoparticles on cellular GSH levels, the intracellular GSH concentration was measured (Fig. 2D). The blank vector had no significant effect on intracellular GSH content. However, treatment with PE NPs led to a 73 % decrease in intracellular GSH concentration, consistent with Erastin's inhibition of System Xc- and subsequent reduction in GSH synthesis in cancer cells. Following exposure to PTFE nanoparticles, the intracellular GSH concentration further decreased by 88 %, indicating that Fe³⁺ caused the Fenton effect, leading to an additional depletion of intracellular GSH. These findings indicated that Erastin and Fe³⁺ acted synergistically to induce ferroptosis in pancreatic cancer cells. Additionally, the expression levels of intracellular GPX4 were measured by Western blot (Fig. 2E and F). Since Erastin did not affect System Xc-expression, the nanoparticles did not have a significant impact on the SLC7A11 protein expression in KPC1199 cells. However, GPX4 expression was notably reduced following nanoparticle treatment, particularly in the PTFE group, consistent with the decrease in GSH levels.

In addition, we measured intracellular ROS production using a reactive oxygen probe (Fig. 2G), which was also analyzed semiquantitatively (Fig. 2H). The control cells showed a low background level of ROS with very weak fluorescence. Both the PTF and PE groups exhibited moderate green fluorescence, attributed to the iron-induced Fenton reaction and Erastin-induced ferroptosis, respectively. Remarkably, the PTFE group showed a further increase in fluorescence signal, confirming the synergistic effect of these two mechanisms. Excessive ROS lead to the oxidation of polyunsaturated fatty acids (PUFA) in lipid membranes, resulting in the formation of intracellular lipid peroxides (LPO), which disrupt cell structure and integrity. Therefore, intracellular LPO accumulation was measured using the BODIPY-C11 fluorescent probe (Fig. 2I) and analyzed semiquantitatively (Fig. 2J and K). The shift in fluorescence from red to green indicated that the unsaturated butadiene moiety of BODIPY-C11 undergoes a redox reaction with ROS within the cell membrane. All nanoparticle formulations showed different levels of LPO accumulation, with the PTFE group demonstrating the strongest effect. Thus, the *in vitro* results indicate that PTFE nanoparticles possess potent antitumor activity. Their enhanced effect is due to the synergistic action of Erastin-induced ferroptosis and Fe³⁺-mediated Fenton reaction, both of which lead to lipid peroxidation and cellular ferroptosis.

2.3. Deep penetration of PTFE into multicellular tumor spheroids

At the cellular level, PTFE nanoparticles exhibited promising responsiveness to KPC1199 pancreatic cancer cells *in vitro*. However, the translation of effective cellular responses to *in vivo* efficacy, particularly in pancreatic cancer, poses challenges due to the dense extracellular matrix (ECM) prevalent in the tumor microenvironment [32–34]. The ECM is predominantly composed of tumor-associated fibroblasts (TAFs) and the collagen they produce upon activation. This dense ECM hinders the efficient transportation and deep penetration of drugs into the tumor interior, often resulting in limited therapeutic effects. Activation of TAFs is primarily mediated by transforming growth factor β (TGF- β) secreted by M2-type tumor-associated macrophages (TAMs) [35,36]. Therefore, to enhance drug penetration into tumors, the ECM needs to be modulated. Encouragingly, polarization of TAMs into M1 macrophages has been reported to reduce TGF- β secretion, offering a potential strategy to promote deep penetration of nanoparticles [37].

To explore this potential, we first investigated the effect of PTFE nanoparticles on macrophage polarization. In the tumor microenvironment, macrophages are predominantly polarized into the M2 phenotype, which supports tumor growth by suppressing the immune system and promoting angiogenesis [38]. To simulate this condition, macrophages were pretreated with IL-4 to induce M2 polarization, as evidenced by a

significant upregulation of CD206, an M2 biomarker (Fig. 3A and B). It is noteworthy that PE alone had little effect on M2-type macrophage polarization as shown by flow cytograms with immunofluorescence images (Fig. 3C, D, S2). In contrast, both PTF and PTFE promoted the polarization of M2-type macrophages to M1-type. This effect may be driven by the intracellular production of ROS induced by iron. Specifically, the proposed mechanism involves iron treatment enhancing MAPK expression, which leads to the phosphorylation of kinase 2 (MK2). This phosphorylation triggers the production of TNF- α , which continues to stimulate macrophages to produce large amounts of ROS, thereby promoting M1-type polarization [39,40]. Remarkably, PTFE nanoparticles demonstrated the most pronounced effect in repolarizing macrophages towards the M1 phenotype and decreasing TGF- β secretion (Fig. 3E).

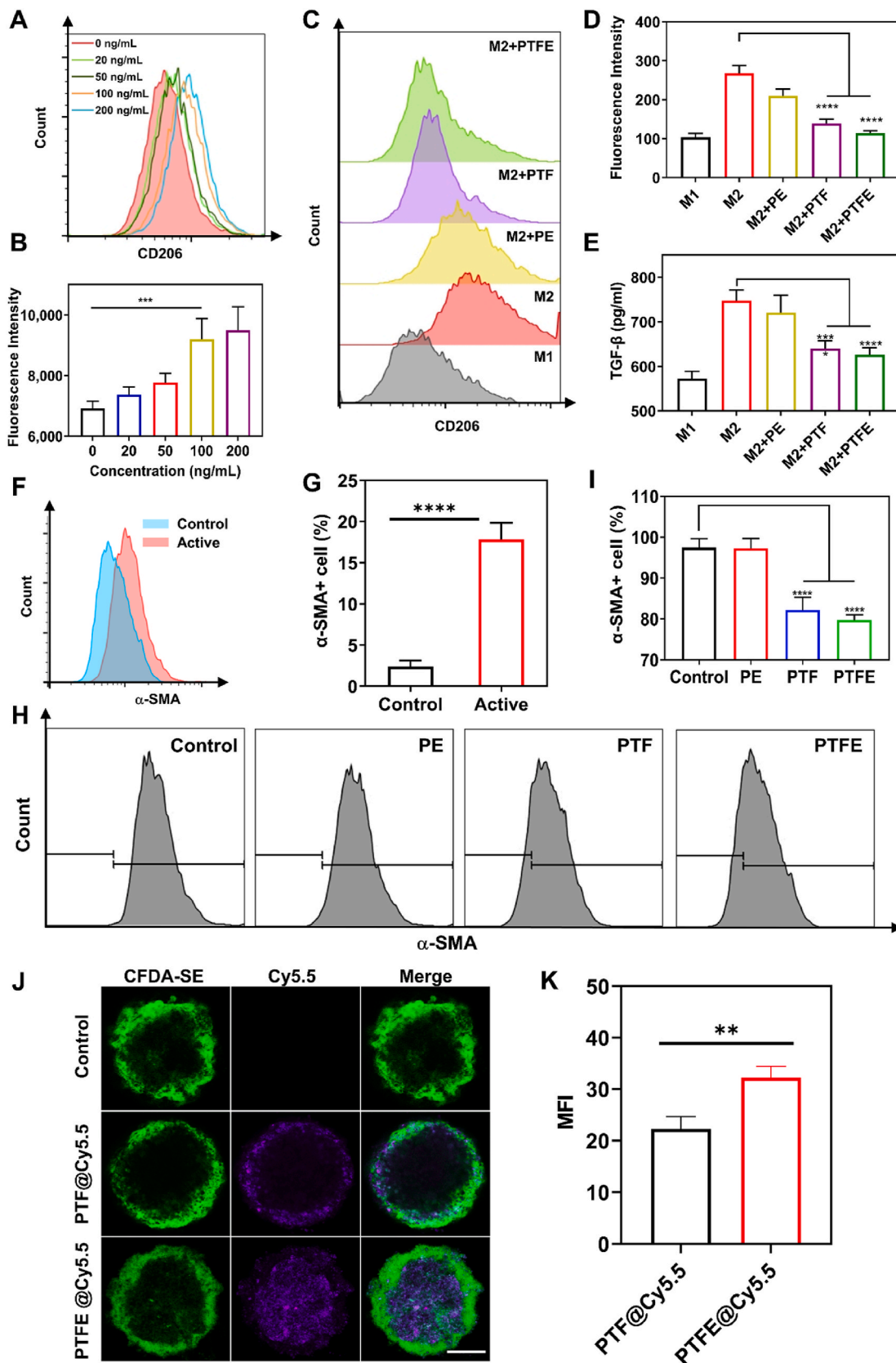
As TGF- β plays a key role in fibroblast activation, we assessed fibroblast activation using the α -SMA biomarker. Culture supernatants from M2 macrophages were incubated with fibroblasts, resulting in a significant increase in α -SMA positive cells, indicating fibroblast activation (Fig. 3F and G). However, when M2 macrophages were pretreated with PTF and PTFE nanoparticles before incubation with fibroblasts, the rate of α -SMA positive expression was reduced (Fig. 3H and I), suggesting that PTFE's capability to repolarize macrophages can mitigate fibroblast activation and enhance nanoparticle penetration into the tumor tissue.

To validate this hypothesis, we developed a multicellular spheroid model comprising KPC1199 tumor cells and NIH3T3 fibroblasts to mimic the microenvironment of pancreatic solid carcinoma. The outer layer of fibroblasts was labeled with green fluorescence. To track nanoparticle penetration, a violet fluorescent Cy5.5 dye was co-loaded into the nanoparticles (Fig. 3J). After 24 h of incubation, PTF nanoparticles were primarily distributed at the outer cells of the bilayer cell tumor spheres. In contrast, the PTFE group displayed numerous violet fluorescence signals throughout the center of the bilayer cell tumor spheres. The fluorescence signal was semi-quantified (Fig. 3K), and it was found that the penetration of PTFE in the three-dimensional tumor spheres increased significantly. This observation suggests that PTFE nanoparticles have a unique capacity for deep penetration into tumor tissue, potentially attributed to the M2-to-M1 macrophage polarization, leading to inhibited fibroblast activation. These findings offer insights into the mechanisms underlying PTFE's enhanced tumor penetration, making it a promising candidate for overcoming the challenges posed by the dense ECM in pancreatic cancer treatment.

2.4. The tumor penetration effect of PTFE in pancreatic mice tumor model

Having demonstrated the deep penetration of PTFE nanoparticles into tumor spheroids *in vitro* and the underlying mechanism, we proceeded to investigate their *in vivo* tumor penetration effect. For this purpose, we established a pancreatic cancer model with a mesenchymal-rich subcutaneous tumor by transplanting C57BL/6 mice with the pancreatic cancer cell line KPC1199 and fibroblast-like cells NIH3T3. When the tumor size reached approximately 150 mm³, Cy5.5-labeled nanoparticles were intravenously administered to the mice. After the therapy, the mice were sacrificed, and tumor tissues were collected for direct observation. Fluorescence imaging of tumor frozen sections revealed that the Cy5.5 signals in the PTF group were mainly limited to the edges of the tumor sections (Fig. 4A). In contrast, the PTFE NPs group exhibited stronger signals that extended deeper into the tumor tissues, corroborating the enhanced tumor penetration ability of PTFE nanoparticles, consistent with the *in vitro* tumor spheroid results.

To elucidate the underlying mechanism *in vivo*, we first investigated the nanoparticles' capability to promote macrophage polarization. Tumor-associated macrophages were co-stained with CD80 (red, an M1 marker) and CD206 (green, an M2 marker). In the control group, the tumor tissue showed intense green fluorescence while the red fluorescence was rather weak (Fig. 4B), indicating predominant polarization of macrophages into the M2 phenotype, indicative of an immune



(caption on next page)

Fig. 3. Deep penetration of PTFE into multicellular tumor spheroids and the underlining mechanisms. (A) Flow analysis plots of M2-type macrophage polarization and (B) their relative semi-quantitative results after different concentrations of IL-4-treated M0-type macrophages. (C) Flow cytometric analysis of CD206 expression in M2-type macrophages under different treatments. Macrophages were pretreated with IL-4 to induce M2 polarization and then exposed to different nanoparticles. (D) Quantification of the fluorescence intensity representing CD206 expression. (E) Measurement of TGF- β secretion in M2-type macrophages under different nanoparticle treatments ($n = 3$). (F) Flow cytometry analysis of fibroblast α -SMA expression after incubation with culture supernatants from M2 macrophages. (G) Corresponding quantitative results of α -SMA expression in fibroblasts. (H) Flow cytometric analysis of fibroblast α -SMA expression following indirect inhibition by nanoparticles ($n = 3$). The nanoparticles were used to pretreat M2 macrophages before incubation with fibroblasts. (I) Corresponding quantitative results of α -SMA expression in fibroblasts. (J) Fluorescence imaging showing the penetration of nanoparticles into bilayer tumor spheres. Scale bar: 100 μm (K) Fluorescence semi-quantitative data of tumor ball nanoparticles per unit area ($n = 3$). Significant differences compared to the control group are indicated as **** $p < 0.0001$ and **** $p < 0.001$.

suppressive microenvironment. After nanoparticle treatments, the red fluorescence representing M1 macrophages intensified, concomitant with a decrease in green signal. Particularly, the PTFE group exhibited the most significant efficacy in promoting M1 macrophage polarization. This finding indicates that the presence of Fe^{3+} alone (for PTF) or Erastin (for PE) alone does not have a noticeable effect on M1 macrophage polarization, but their combined presence in PTFE nanoparticles synergistically increases the number of M1 macrophages. Western blot and flow cytometry further confirmed the expression of CD80 and CD206 in macrophages (Fig. 4C–F), and consistent outcomes were obtained, substantiating the nanoparticles' potential to induce M1 macrophage polarization. In line with this result, TGF- β secretion in the tumor tissue was significantly lower in the PTF-treated and PTFE-treated groups compared to the control group (Fig. 4G).

Furthermore, we assessed the location and intensity of fibroblast activation in the cancer tissue by immunofluorescence detection of the fibroblast activation marker α -SMA (Fig. 4H). The control group exhibited the highest level of fibroblast activation, with dispersed and thick, regular outer layers and a more sparse interior structure. The PE-treated group still showed activated fibroblasts with a thick, regular outer layer, but their number was reduced. In the PTF-treated group, the number of activated fibroblasts was even lower, and their arrangement became disorganized, indicating the inhibitory impact of PTF on fibroblast activation. Notably, the PTFE-treated group exhibited a significantly lower number of activated fibroblasts with a disorganized distribution. Furthermore, the deposition of collagen, a protein that is synthesized by activated fibroblasts and abundant in dense extracellular matrix, was quantified (Fig. 4I). Sirius scarlet staining confirmed that the PTFE group had the lowest collagen expression due to the suppression of fibroblast activation. Thus, PTFE nanoparticles effectively alter the stromal microenvironment by promoting M1 macrophage polarization, decreasing TGF- β secretion, inhibiting fibroblast activation, and reducing collagen fiber deposition, which collectively contribute to their enhanced tumor penetration compared to PTF.

2.5. *In vivo* anti-tumor effect of the nanoparticles

After establishing the potent ferroptosis-inducing capability and significant tumor cell penetration of PTFE, we proceeded to evaluate its anti-tumor efficacy *in vivo*. When the tumor size reached approximately 100 mm^3 , the mice were randomly divided into different treatment groups and received various nanoparticle treatments every three days for a total of five doses (Fig. 5A). We monitored the tumor volume every other day to dynamically evaluate therapeutic efficacy. Both PTF and PE nanoparticles exhibited some tumor inhibitory effect compared to the control (Fig. 5B). This can be attributed to their respective ability to induce the Fenton reaction and initiate ferroptosis in tumor cell, however their tumor suppression effect was poor. Through previous studies, it was found that good therapeutic effects could not be achieved either by delivering iron alone to increase the content of unstable intracellular iron pools [27,41], or by delivering Erastin alone to disrupt the redox balance and induce ferroptosis [42,43]. However, delivering both at the same time resulted in the most significant anti-tumor efficacy in the PTFE group due to the combined effect of their dual anti-tumor mechanisms. In addition, the improvement of tumor penetration ability also

contributed. To directly observe the impact of the nanoparticle treatments on tumor tissues, we collected the tumor samples after the treatment period (Fig. 5C and D). Specifically, PTFE nanoparticles achieved an impressive tumor inhibition rate of 75 %. To validate the enhanced tumor penetration effect of PTFE NPs, tumor tissues were subjected to H&E staining (Fig. 5E). The control group exhibited dense tumor structure, prominent inflammatory cell infiltration, and evident outer fibroblast texture characteristic of a tumor inflammatory microenvironment. Treatment with the blank carrier PTF nanoparticles resulted in a reduction in fibroblast texture but did not lead to significant therapeutic efficacy, indicating that Fe^{3+} alone had limited impact. In contrast, PE-treated tumors showed a sparser structure, attributable to the anti-tumor effect of Erastin as a ferroptosis inducer. Notably, the PTFE-treated group displayed apparent nuclear necrosis and cavities, demonstrating a highly effective anti-tumor outcome. To further confirm the efficacy, the mice survival rate was recorded after various treatments (Fig. 5F). Compared with the control group, the 50 % survival rate of the carrier PTF group was 27 days, and the 50 % survival rate of the Erastin group was extended to 30 days, which may be because Erastin broke the Redox balance in the tumor, resulting in the accumulation of oxidative stress, and had a certain inhibitory effect on tumor cells. On the other hand, PTFE still had a survival rate of 62.5 % at 40 days, demonstrating the improved efficacy.

To elucidate the anti-tumor mechanism of PTFE NPs *in vivo*, we measured the content of malondialdehyde (MDA), a lipid peroxidation product, in tumor tissues to assess the extent of membrane lipid peroxidation (Fig. 5G). The PTFE-NP group exhibited significantly higher MDA content than the control group, indicating a strong induction of membrane lipid peroxidation. Additionally, the concentration of GSH in cancer tissues significantly decreased following treatment, with the PTFE group showing the most pronounced effect (Fig. 5H). This decrease in GSH can be attributed to the inhibition of the System Xc-, leading to reduced synthesis and continuous depletion of intracellular antioxidants. We further examined the expression of GPX4 protein (Fig. 5I), which was found to be lowest in the PTFE group, indicating successful inhibition of the System Xc-transporter. This reduction in GPX4 protein expression disrupts intracellular redox homeostasis and exacerbates oxidative stress in tumor cells. These findings collectively demonstrate the potent anti-tumor effects of PTFE NPs *in vivo*, mediated by their dual ferroptosis induction and enhanced tumor penetration capabilities.

2.6. Safety evaluation of the nanoparticles

Finally, the safety evaluation of the nanomedicine was carried out to assess its potential toxicity and biocompatibility. In the hemolysis test, all types of nanoparticles demonstrated a hemolytic rate of less than 50 %, indicating their hemocompatibility and suitability for intravenous administration (Fig. 6A). During the treatment period, the body weights of the mice were regularly monitored (Fig. 6B). Throughout the study, the body weights of the mice in each treatment group showed normal fluctuations with age, and no significant changes or noticeable abnormalities were observed. To further assess potential organ toxicity, blood biochemical indicators, including serum AST, ALT, BUN, and CRE levels, were measured in mice from each treatment group (Fig. 6C and D). The results revealed that the nanoparticles did not cause hepatotoxicity or

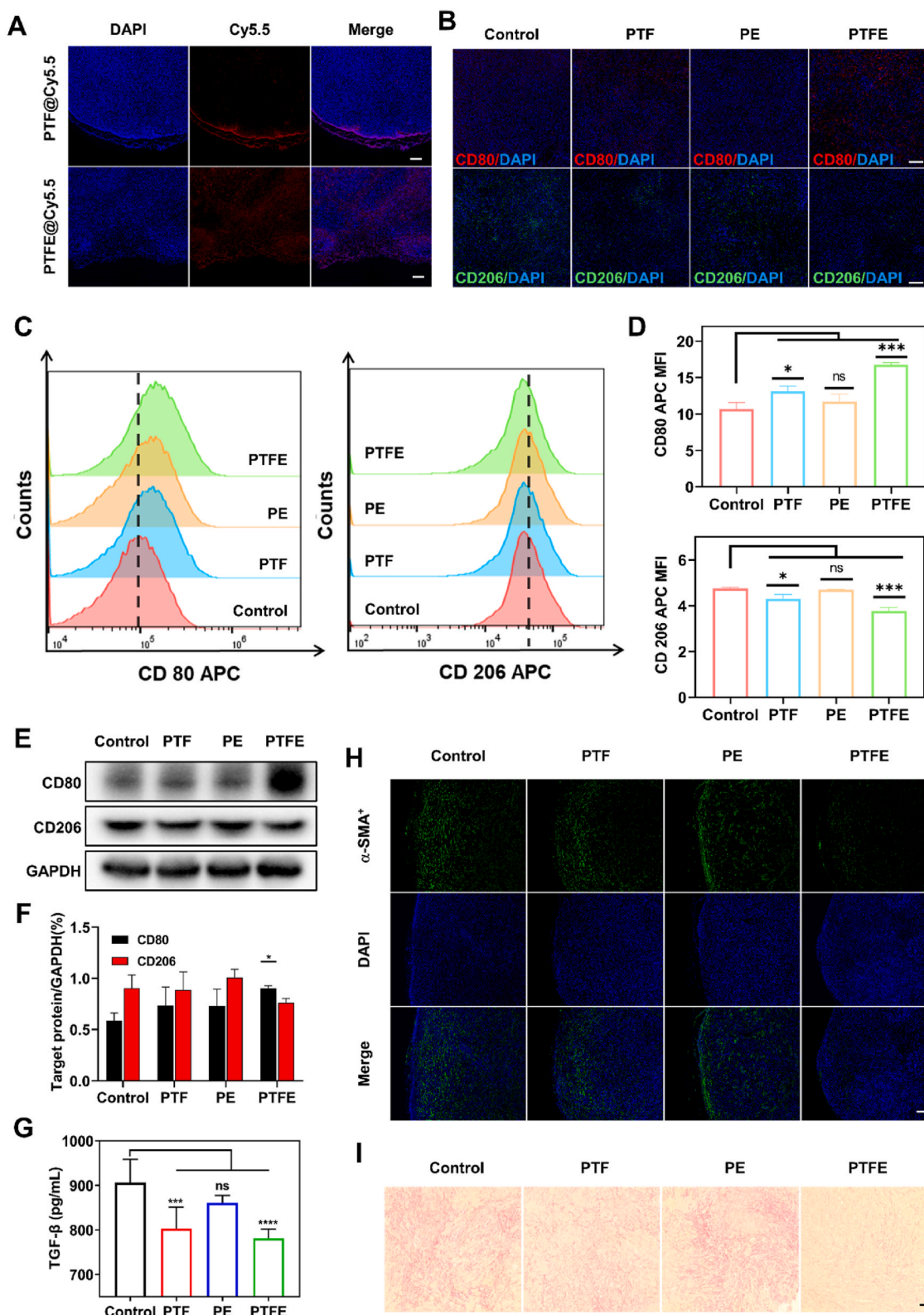


Fig. 4. The tumor penetration effect in vivo. (A) Image of tissue penetration of nanoparticles in tumor tissue. Scale bar: 200 μ m. (B) Immunofluorescence staining of tumor sections showing macrophage polarization. Macrophages were co-stained with CD80 (red, M1 marker) and CD206 (green, M2 marker). Scale bar: 200 μ m. (C) Flow cytometric analysis of CD80 and CD206 expression in tumor tissue. (D) Relative quantitative results from C (n = 5). (E) Western blot analysis of CD206 and CD80 protein expression in tumor tissues. (F) Relative quantitative results of CD206 and CD80 expression. (n = 3). (G) Measurement of TGF- β content in tumor tissues. (n = 5). (H) Immunofluorescence images of α -SMA fibroblasts in tumor tissue. Scale bar: 200 μ m. (I) Picrosirius red staining of collagen fibers in tumor tissue. Scale bar: 200 μ m. Significant differences compared to the control group are indicated as *P < 0.1, **P < 0.01, ***P < 0.001 and ****P < 0.0001.

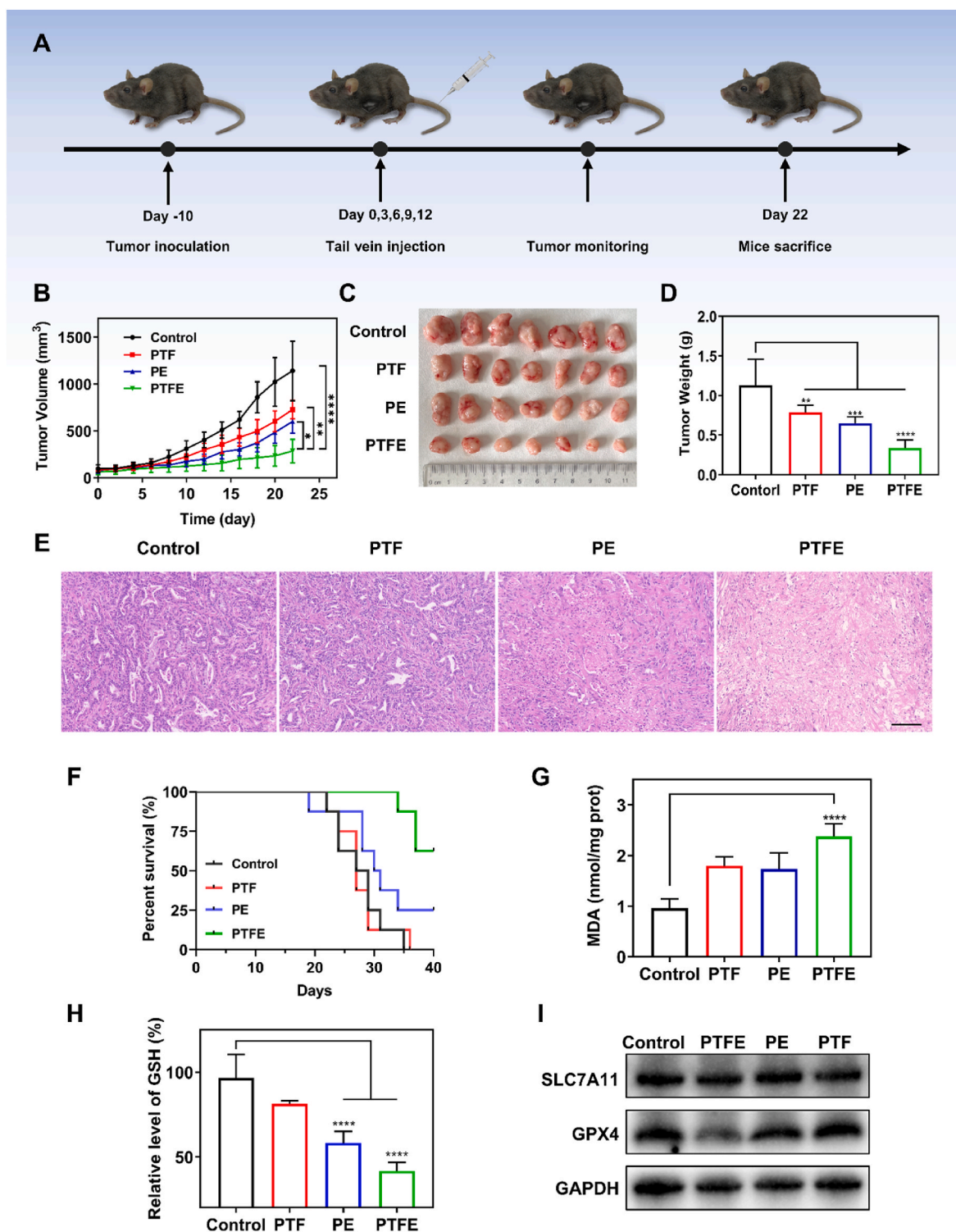


Fig. 5. In Vivo Anti-tumor Effect. (A) Schematic illustration depicting the experimental procedure of the animal studies. (B) Tumor growth curve, displaying the dynamic changes in tumor volume over time. (C) Representative images showing tumors isolated after different treatments. (D) Statistical analysis of tumor weight isolated after various treatments ($n = 7$). (E) Hematoxylin and eosin (H&E) staining of tumor tissue sections, providing visual insights into the tumor microenvironment. (Scale bar: 100 μm). (F) The survival curves. Shows survival of mice after drug administration ($n = 8$). (G) Measurement of MDA levels in tumor tissues ($n = 5$). (H) Quantification of GSH levels in tumor tissues ($n = 5$). (I) Expression levels of SLC7ALL and GPX4 proteins in tumor tissues, evaluated through Western blot analysis. Significant differences compared to the control group are indicated as $**p < 0.01$, $***p < 0.001$ and $****p < 0.0001$.

nephrotoxicity, as there were no significant alterations in the blood biochemical parameters. Additionally, major organs from each treatment group were subjected to histological examination through H&E staining (Fig. 6E). Importantly, all major organs exhibited normal

histological features without any noticeable morphological abnormalities, indicating the absence of acute organ toxicity. Taken together, the nanoparticles used in this study have a satisfactory safety profile for in vivo applications, which is promising for its potential clinical

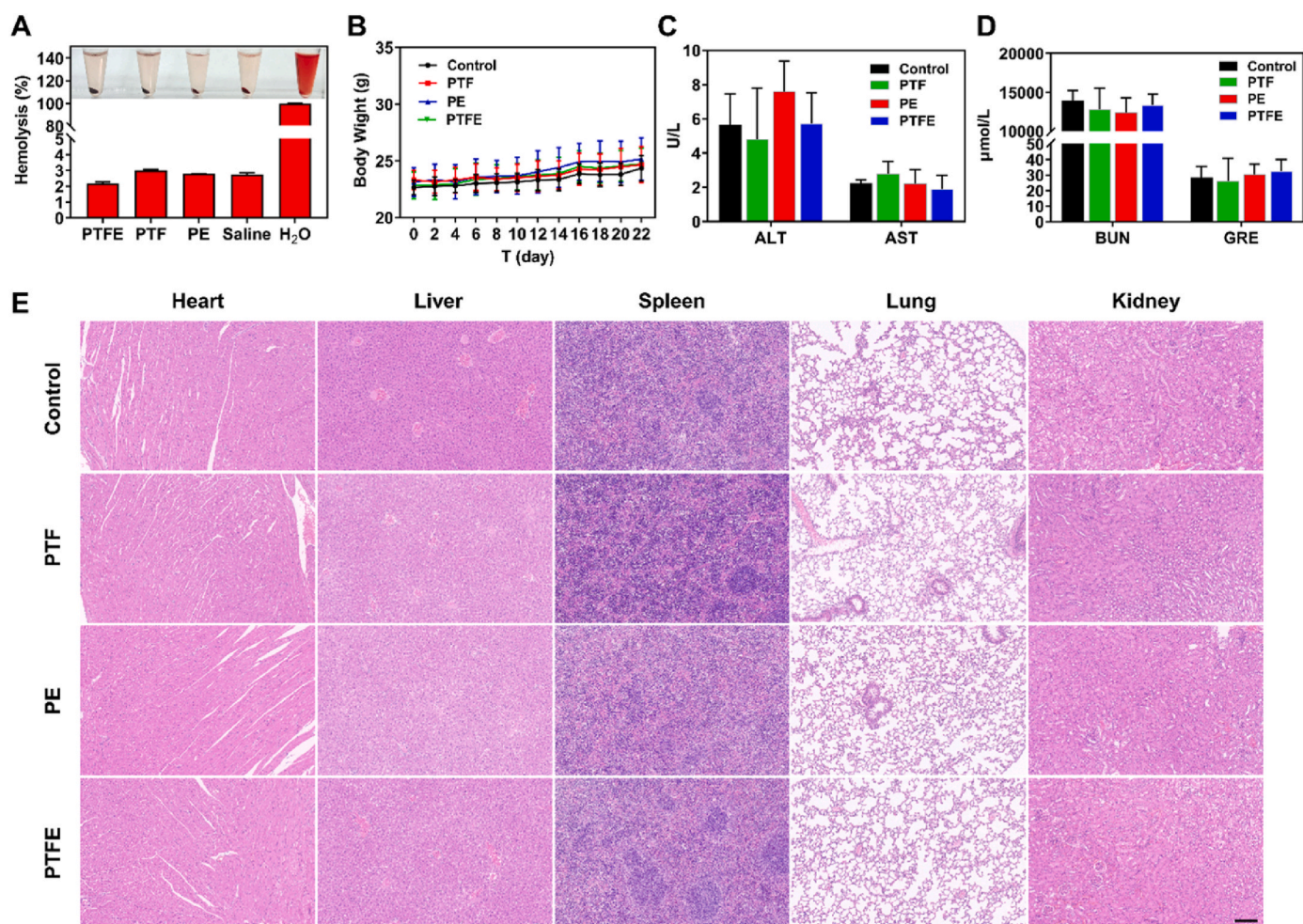


Fig. 6. Safety evaluation of the nanomedicine. (A) Hemolysis rate and microscopic observation of red blood cell hemolysis ($n = 3$). (B) Body weight change curves of mice in different treatment groups ($n = 7$). (C) Serum levels of AST and ALT, and (D) BUN and CRE in mice from different treatment groups ($n = 7$). (E) Representative H&E staining sections of major organs including heart, liver, spleen, lung, and kidney from mice treated with different preparations. (Scale bar: 100 μm).

translation.

3. Conclusion

In conclusion, our study introduces a novel iron-containing nanoparticle formulation, PTFE, exhibiting dual anti-tumor mechanisms for efficient pancreatic cancer therapy. PTFE effectively induces the Fenton reaction and ferroptosis, resulting in abundant generation of ROS and accumulation of LOP, ultimately leading to ferroptosis induction and enhanced tumor cell destruction. Moreover, PTFE demonstrates exceptional tumor penetration capabilities, effectively overcoming the formidable barrier posed by the dense tumor stroma. This is achieved through its inherent ability to repolarize M2 macrophages into the M1 phenotype, thereby modulating the tumor microenvironment, including fibroblast activation and collagen deposition. In preclinical studies, PTFE exhibits remarkable anti-tumor efficacy, leading to significant suppression of pancreatic tumor growth. Crucially, the administration of PTFE is well-tolerated in vivo, demonstrating no noticeable toxicity during treatment. These findings underscore the promising potential of PTFE as an effective nanomedicine platform for pancreatic cancer therapy.

CRedit authorship contribution statement

Aiping Huang: Methodology, Formal analysis, Data curation, Conceptualization. **Qingnian Li:** Writing – original draft, Visualization,

Validation, Methodology. **Xinyi Shi:** Methodology. **Junyi Gao:** Methodology. **Yiran Ma:** Investigation. **Jinsong Ding:** Supervision, Resources. **Surong Hua:** Writing – review & editing, Supervision, Conceptualization. **Wenhu Zhou:** Writing – review & editing, Resources, Project administration, Formal analysis, Conceptualization.

Declaration of competing interest

The authors declare no conflict of interest.

Data availability

Data will be made available on request.

Acknowledgments

This work was supported by Natural Science Foundation of Hunan province in China (2021JJ20084), and the Science and Technology Innovation Program of Hunan Province (2021RC3020).

Appendix A. Supplementary data

Supplementary data to this article can be found online at <https://doi.org/10.1016/j.mtbio.2024.101132>.

References

- [1] A. Moore, T. Donahue, Pancreatic cancer, *JAMA* 322 (14) (2019) 1426–26.
- [2] C.J. Halbrook, C.A. Lyssiotis, D.I. Pasca, M. Magliano, et al., Pancreatic cancer: advances and challenges, *Cell* 186 (8) (2023) 1729–1754.
- [3] M. Wang, Z. Guo, J. Zeng, et al., Bio-assembled smart nanocapsules for targeted delivery of KRAS shRNA and cancer cell bioimage, *Chin. Chem. Lett.* 34 (1) (2023) 107651.
- [4] S. Anthiya, S.C. Öztürk, H. Yanik, et al., Targeted siRNA lipid nanoparticles for the treatment of KRAS-mutant tumors, *J. Contr. Release* 357 (2023) 67–83.
- [5] L. Qiang, M.T. Hoffman, L.R. Ali, et al., Transforming growth factor- β blockade in pancreatic cancer enhances sensitivity to combination chemotherapy, *Gastroenterology* 165 (4) (2023) 874–90.e10.
- [6] Y. Lan, M. Moustafa, M. Knoll, et al., Simultaneous targeting of TGF- β /PD-L1 synergizes with radiotherapy by reprogramming the tumor microenvironment to overcome immune evasion, *Cancer Cell* 39 (10) (2021) 1388, 403.e10.
- [7] Y. Song, Y. Huang, F. Zhou, et al., Macrophage-targeted nanomedicine for chronic diseases immunotherapy, *Chin. Chem. Lett.* 33 (2) (2022) 597–612.
- [8] A.N. Hosen, R.A. Brekken, A. Maitra, Pancreatic cancer stroma: an update on therapeutic targeting strategies, *Nat. Rev. Gastroenterol. Hepatol.* 17 (8) (2020) 487–505.
- [9] X. Chen, F. Jia, Y. Li, et al., Nitric oxide-induced stromal depletion for improved nanoparticle penetration in pancreatic cancer treatment, *Biomaterials* 246 (2020) 119999.
- [10] H. Chen, H. Song, Y. Luo, et al., Transcytosis mediated deep tumor penetration for enhanced chemotherapy and immune activation of pancreatic cancer, *Adv. Funct. Mater.* 33 (28) (2023) 2214937.
- [11] B.-P. Miriam, G.-C. Rocio, L. Berta, et al., VCN-01 disrupts pancreatic cancer stroma and exerts antitumor effects, *J. ImmunoTher Cancer* 9 (11) (2021) e003254.
- [12] D. Wu, X. Chen, J. Zhou, et al., A synergistic optical strategy for enhanced deep-tumor penetration and therapy in the second near-infrared window, *Mater. Horiz.* 7 (11) (2020) 2929–2935.
- [13] B. Chen, W. Dai, D. Mei, et al., Comprehensively priming the tumor microenvironment by cancer-associated fibroblast-targeted liposomes for combined therapy with cancer cell-targeted chemotherapeutic drug delivery system, *J. Contr. Release* 241 (2016) 68–80.
- [14] S. Bisht, M. Mizuma, G. Feldmann, et al., Systemic administration of polymeric nanoparticle-encapsulated curcumin (NanoCurc) blocks tumor growth and metastases in preclinical models of pancreatic cancer, *Mol. Cancer Therapeut.* 9 (8) (2010) 2255–2264.
- [15] Y. Chen, Y. Huang, S. Zhou, et al., Tailored chemodynamic nanomedicine improves pancreatic cancer treatment via controllable damaging neoplastic cells and reprogramming tumor microenvironment, *Nano Lett.* 20 (9) (2020) 6780–6790.
- [16] X. Cui, J. Chen, M. Li, et al., Tumor-associated fibroblast-targeted regulation and deep tumor delivery of chemotherapeutic drugs with a multifunctional size-switchable nanoparticle, *ACS Appl. Mater. Interfaces* 11 (43) (2019) 39545–39559.
- [17] Y.J. Wang, F.M. Chen, H.L. Zhou, et al., Redox dyshomeostasis with dual stimuli-activatable dihydroartemisinin nanoparticles to potentiate ferroptotic therapy of pancreatic cancer, *Small Methods* 7 (5) (2023) 2200888.
- [18] Z. Yao, Q. Hu, P. Jin, et al., A self-assembly combined nano-prodrug to overcome gemcitabine chemo-resistance of pancreatic tumors, *Adv. Funct. Mater.* 33 (30) (2023) 2214598.
- [19] X. Chen, R. Kang, G. Kroemer, et al., Targeting ferroptosis in pancreatic cancer: a double-edged sword, *Trends in Cancer* 7 (10) (2021) 891–901.
- [20] A. Butler, R.M. Theisen, Iron(III)-siderophore coordination chemistry: reactivity of marine siderophores, *Coord. Chem. Rev.* 254 (3) (2010) 288–296.
- [21] W.S. Yang, R. Sriramaratnam, M.E. Welsch, et al., Regulation of ferroptotic cancer cell death by GPX4, *CELL* 156 (1–2) (2014) 317–331.
- [22] Y. He, Y. Ling, Z. Zhang, et al., Butyrate reverses ferroptosis resistance in colorectal cancer by inducing c-Fos-dependent xCT suppression, *Redox Biol.* 65 (2023) 102822.
- [23] B. Gan, How erastin assassinates cells by ferroptosis revealed, *Protein & Cell* 14 (2) (2023) 84–86.
- [24] M.A. Badgley, D.M. Kremer, H.C. Maurer, et al., Cysteine depletion induces pancreatic tumor ferroptosis in mice, *Science* 368 (6486) (2020) 85–89.
- [25] S.L. Cramer, A. Saha, J. Liu, et al., Systemic depletion of L-cyst(e)ine with cyst(e)inase increases reactive oxygen species and suppresses tumor growth, *Nat. Med.* 23 (1) (2017) 120–127.
- [26] J. Guo, P. Liu, B. Wei, et al., Reversing the negative effect of adenosine A1 receptor-targeted immunometabolism modulation on melanoma by a co-delivery nanomedicine for self-activation of anti-PD-L1 DNzyme, *Nano Today* 48 (2023) 101722.
- [27] P. Liu, X. Shi, Y. Peng, et al., Anti-PD-L1 DNzyme loaded photothermal Mn2+/Fe3+ hybrid metal-phenolic networks for cyclically amplified tumor ferroptosis-immunotherapy, *Adv. Healthcare Mater.* 11 (8) (2022) 2102315.
- [28] L. Guo, S. Zhong, P. Liu, et al., Radicals scavenging MOFs enabling targeting delivery of siRNA for rheumatoid arthritis therapy, *Small* 18 (27) (2022) 2202604.
- [29] P. Liu, X. Liu, Y. Cheng, et al., Core-shell nanosystems for self-activated drug-gene combinations against triple-negative breast cancer, *ACS Appl. Mater. Interfaces* 12 (48) (2020) 53654–53664.
- [30] L. Guo, Y. Chen, T. Wang, et al., Rational design of metal-organic frameworks to deliver methotrexate for targeted rheumatoid arthritis therapy, *J. Contr. Release* 330 (2021) 119–131.
- [31] R. Liu, C. Luo, Z. Pang, et al., Advances of nanoparticles as drug delivery systems for disease diagnosis and treatment, *Chin. Chem. Lett.* 34 (2) (2023) 107518.
- [32] T. Guo, X. Liu, Z. Zhang, et al., A recombinant Newcastle disease virus expressing MMP8 promotes oncolytic efficacy, *Chin. Chem. Lett.* 32 (12) (2021) 3962–3966.
- [33] W. Chen, Y. Yuan, C. Li, et al., Modulating tumor extracellular matrix by simultaneous inhibition of two cancer cell receptors, *Adv. Mater.* 34 (10) (2022) 2109376.
- [34] Z. Li, X. Shan, Z. Chen, et al., Applications of surface modification technologies in nanomedicine for deep tumor penetration, *Adv. Sci.* 8 (1) (2021) 2002589.
- [35] E.S. Glazer, L.F. Reed, C.J. Freeburg, et al., Effect of macrophages on pancreatic cancer, *J. Clin. Oncol.* 36 (4, suppl) (2018) 324, 24.
- [36] T. Murthy, J. Podojil, T. Kwak, et al., Biodegradable nanoparticles inhibit tumor growth by altering tumor-associated macrophages and cancer-associated fibroblasts, *J. Clin. Oncol.* 40 (16, suppl) (2022) e14553 e53.
- [37] E. Lou, J. Xiu, Y. Baca, et al., The tumor microenvironment and immune infiltration landscape of KRAS mutant pancreatic ductal adenocarcinomas (PDAC) compared to colorectal adenocarcinomas (CRC), *J. Clin. Oncol.* 40 (16, suppl) (2022) 4142, 42.
- [38] Y. Zhao, J. Sun, Y. Li, et al., Tryptophan 2,3-dioxygenase 2 controls M2 macrophages polarization to promote esophageal squamous cell carcinoma progression via AKT/GSK3 β /IL-8 signaling pathway, *Acta Pharm. Sin.* B 11 (9) (2021) 2835–2849.
- [39] B. Tang, Y. Wang, W. Xu, et al., Macrophage xCT deficiency drives immune activation and boosts responses to immune checkpoint blockade in lung cancer, *Cancer Lett.* 554 (2023) 216021.
- [40] Z. Gu, T. Liu, J. Tang, et al., Mechanism of iron oxide-induced macrophage activation: the impact of composition and the underlying signaling pathway, *J. Am. Chem. Soc.* 141 (15) (2019) 6122–6126.
- [41] M. Mu, X. Liang, N. Zhao, et al., Boosting ferroptosis and microtubule inhibition for antitumor therapy via a carrier-free supermolecule nanoreactor, *J. Pharm Anal* 13 (1) (2023) 99–109.
- [42] A.M. Battaglia, A. Sacco, I.D. Perrotta, et al., Iron administration overcomes resistance to erastin-mediated ferroptosis in ovarian cancer cells, *Front. Oncol.* 12 (2022).
- [43] X. Guo, Y. Guo, J. Li, et al., Arginine expedites erastin-induced ferroptosis through fumarate [J/OL] 24 (19) (2023), <https://doi.org/10.3390/ijms241914595>.